

A kernel-based method for coarse graining complex dynamical systems

Andreas Bittracher¹, Stefan Klus¹,
Boumediene Hamzi^{2,3}, and Christof Schütte^{1,4}

¹Department of Mathematics and Computer Science, Freie Universität Berlin, Germany

²Department of Mathematics, Imperial College London, London, UK

³AlFaisal University, Riyadh, KSA

⁴Zuse Institute Berlin, Germany

Abstract

We present a novel kernel-based machine learning algorithm for identifying the low-dimensional geometry of the effective dynamics of high-dimensional multiscale stochastic systems. Recently, the authors developed a mathematical framework for the computation of optimal reaction coordinates of such systems that is based on learning a parametrization of a low-dimensional transition manifold in a certain function space. In this article, we enhance this approach by embedding and learning this transition manifold in a reproducing kernel Hilbert space, exploiting the favorable properties of kernel embeddings. Under mild assumptions on the kernel, the manifold structure is shown to be preserved under the embedding, and distortion bounds can be derived. This leads to a more robust and more efficient algorithm compared to previous parametrization approaches.

1. Introduction

Many of the dynamical processes investigated in the sciences today are characterized by the existence of phenomena on multiple, interconnected time scales that determine the long-term behavior of the process. Examples include the inherently multiscale dynamics of atmospheric vortex- and current formation which needs to be considered for effective weather prediction [24, 29], or the vast difference in time scales on which bounded atomic interactions, side-chain interactions, and the resulting formation of structural motifs occur in biomolecules [19, 12, 10]. An effective approach to analyzing these systems is often the identification of a low-dimensional observable of the system that captures the interesting behaviour on the longest time scale. However, the computerized identification of such observables from simulation data poses a significant computational challenge, especially for high-dimensional systems.

Recently, the authors have developed a novel mathematical framework for identifying such essential observables for the slowest time scale of a system [6]. The method—called the *transition manifold approach*—was primarily motivated by molecular dynamics, where the dynamics is typically described by a thermostated Hamiltonian system or diffusive motion

in molecular dynamics landscapes. In these systems, local minima of the potential energy landscape induce *metastable behavior*, which is the phenomenon that on long time scales, the dynamics is characterized by rare transitions between certain sets that happen roughly along interconnecting *transition pathways* [35, 41, 17]. The sought-after essential observables should thus resolve these transition events, and are called *reaction coordinates* in this context [46, 4], a notion that we will adopt here. Despite of its origins, the transition manifold approach is also applicable to other classes of reducible systems (which will also be demonstrated in this article).

At the heart of this approach is the insight that good reaction coordinates can be found by parametrizing a certain *transition manifold* \mathbb{M} in the function space L^1 . This manifold has strong connections to the aforementioned transition pathway [5], but is not equivalent. Its defining property is that, for times τ that fall between the fastest and slowest time scales, the *transition density functions* with relaxation time τ concentrate around \mathbb{M} . The algorithmic strategy to parametrize \mathbb{M} can then be summarized as

1. Choose test points in the dynamically relevant regions of the state space.
2. Sample the transition densities for each test point by Monte Carlo simulation.
3. Embed the transition densities into a Euclidean space by a generic embedding function.
4. Parametrize the embedded transition densities with the help of established manifold learning techniques.

The result is a reaction coordinate evaluated in the test points. This reaction coordinate has been shown to be as expressive as the dominant eigenfunctions of the transfer operator associated with the system [6], which can be considered an “optimal” reaction coordinate [20, 11, 30]. One decisive advantage of our method, however, is the ability to compute the reaction coordinate *locally* (by choosing the test points), whereas with conventional methods, the inherently global computation of transfer operator eigenfunctions quickly becomes infeasible due to the curse of dimensionality. Kernel-based methods for the computation of eigenfunctions alleviate this problem to some extent [43, 25]. Nevertheless, the number of dominant eigenfunctions critically depends on the number of metastable states, which can be significantly larger than the *natural* dimension of the reaction coordinate [6].

However, the algorithm proposed originally had several shortcomings related to the choice of the embedding function. First, in order to ensure the preservation of the manifold’s topology under the embedding, the dimension of \mathbb{M} had to be known in advance. Second, the particular way of choosing the embedding functions allowed no control over the distortion of \mathbb{M} , which may render the parametrization problem numerically ill-conditioned.

The goal of this article is to overcome the aforementioned problems by *kernelizing* the transition manifold embedding. That is, we present a method to implicitly embed the transition manifold into a *reproducing kernel Hilbert space* (RKHS) with a proper kernel. The RKHS is—depending on the kernel—a high- or even infinite-dimensional function space with the crucial property that inner products between points embedded into it can be computed by cheap kernel evaluations, without ever explicitly computing the embedding [48, 38]. In machine learning, this so-called *kernel trick* is often used to derive nonlinear versions of originally linear algorithms, by interpreting the RKHS-embedding of a data set as a high-dimensional, nonlinear transformation, and (implicitly) applying the linear algorithm to the transformed data. This approach has been successfully applied to methods such as *principal component analysis* (PCA) [40], *canonical correlation analysis* (CCA) [31], and *time-lagged independent*

component analysis (TICA) [43], to name but a few.

Due to their popularity, the metric properties of the kernel embedding are well-studied [45, 21, 47, 22, 34]. In particular, for characteristic kernels, the RKHS is “large” in an appropriate sense, and geometrical information is well-preserved under the embedding. For our application, this means that distances between points on the transition manifold \mathbb{M} are approximately preserved, and thus the distortion of \mathbb{M} under the embedding can be bounded. This will guarantee that the final manifold learning problem is well-posed. Moreover, if the transformation induced by the kernel embedding is able to approximately linearize the transition manifold, there is hope that efficient *linear* manifold learning methods can be used to parametrize the embedded transition manifold.

The main contributions of this work are as follows:

1. We develop a kernel-based algorithm to approximate transition manifolds and compare it with the Euclidean embedding counterpart.
2. We derive measures for the distortion of the embedding and associated error bounds.
3. We illustrate the efficiency of the proposed approach using academic and molecular dynamics examples.

In Section 2, we will formalize the definition of transition manifolds and derive conditions under which systems possess such manifolds. Section 3 introduces kernels and the induced RKHSs. Furthermore, we show that the algorithm to compute transition manifolds numerically can be written purely in terms of kernel evaluations and derive measures for the distortion of the manifold caused by the embedding into the RKHS. Numerical results illustrating the benefits of the proposed kernel-based methods are presented in Section 4 and a conclusion and future work in Section 5.

2. Reaction coordinates based on transition manifolds

In what follows, let $\{X_t\}_{t \geq 0}$ (abbreviated as X_t) be a reversible, thus ergodic, stochastic process on a compact state space $\mathbb{X} \subset \mathbb{R}^n$ and ρ its unique invariant density. That is, if $X_0 \sim \rho$, then $X_t \sim \rho$ for all $t \geq 0$. For $x \in \mathbb{X}$ and $t \geq 0$, let $p_x^t: L^1(\mathbb{X}) \rightarrow L^1(\mathbb{X})$ denote the transition density function of the system, i.e., $p_x^t(y)$ describes the probability of finding the system in y at time t , after starting in x at time 0.

2.1. Reducibility of dynamical systems

We assume the state space dimension n to be large. The main objective of this work is the identification of good low-dimensional *reaction coordinates* (RCs) or *order parameters* of the system. An r -dimensional RC is a smooth map $\xi: \mathbb{X} \rightarrow \mathbb{Y}$ from the full state space \mathbb{X} to a lower-dimensional space $\mathbb{Y} \subset \mathbb{R}^r$, $r \ll n$. Informally, we call such an RC *good* if the long-term dynamics of the projected process $\xi(X_t)$ —i.e., the process observed through the RC—resembles the long-term dynamics of the full process X_t . A quantitative measure for the quality of RCs will follow in Section 2.2.

A geometric characterization of good reaction coordinates based on the so-called *transition manifold* was derived in [6].

Definition 2.1. Let $\tau > 0$ be fixed. The set

$$\tilde{\mathbb{M}} := \{p_x^\tau \mid x \in \mathbb{X}\},$$

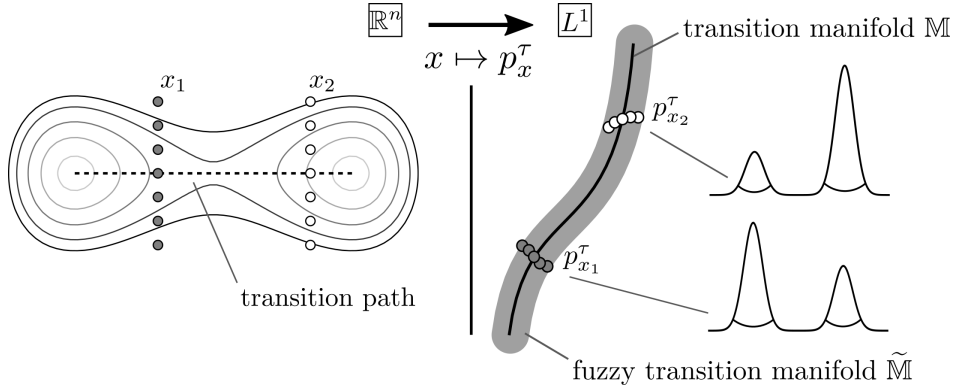


Figure 1: Illustration of the transition manifold concept for metastable systems.

is called the fuzzy transition manifold of the system.

The definition is motivated by the following observation: If the system is in a certain way separable into a slowly equilibrating r -dimensional part and a quickly equilibrating $n - r$ -dimensional part, and τ is chosen to be in a certain intermediate¹ time scale range, then $\tilde{\mathbb{M}}$ approximately forms an r -dimensional manifold in L^1 . Let us illustrate this with the aid of a simple example.

Example 2.2. Consider the process X_t to be described by overdamped Langevin dynamics

$$dX_t = -\nabla V(X_t)dt + \sqrt{2/\beta}dW_t, \quad (1)$$

with the energy potential V , the inverse temperature β , and Brownian motion W_t . The potential depicted in Figure 1 possesses two metastable states, located around the local energy minima. Any realization of this system that started in one of the the metastable sets will likely remain in that set for a long time. Moreover, a realization that started outside of the wells will with high probability quickly leave the transition region and move into one of the two metastable sets. The probability of whether the trajectory will be trapped in the left or right well depends almost exclusively on the horizontal coordinate of the starting point x , or, in other words, the progress of x along the transition path. Thus, for times τ that allow typical trajectories to move into one of the wells, the transition densities p_x^τ also depend only on the horizontal but not the vertical coordinate of x . This means that the fuzzy transition manifold $\tilde{\mathbb{M}}$ essentially forms a one-dimensional manifold in the space of probability densities. Also, any parametrization of this manifold corresponds to a parametrization of the horizontal coordinate, and thus to a good reaction coordinate. \triangle

The concept of (fuzzy) transition manifolds can be made rigorous by the following definition:

Definition 2.3. The process X_t is called (ε, r) -reducible if there exists an r -dimensional manifold $\mathbb{M} \subset \tilde{\mathbb{M}}$ such that for a fixed lag time τ , it holds that

$$\min_{f \in \mathbb{M}} \|f - p_x^\tau\|_{L^2_{1/\rho}} \leq \varepsilon \quad \text{for all } x \in \mathbb{X}.$$

Any such \mathbb{M} is called a transition manifold of the system.

¹Intermediate here means that it has to be large enough so that the fast processes essentially equilibrated but the slow processes are still present and distinguishable.

Two remarks are in order:

1. The fact that we require closeness with respect to the $L^2_{1/\rho}$ -norm, instead of, for example, the L^1 -norm, is indeed important here, as measuring the quality of a given RC will require a certain Hilbert space structure. This will be detailed below; for now, simply note that for all $x \in \mathbb{X}$ it holds that $p_x^t \in L^2_{1/\rho}$ since $L^1 \subset L^2_{1/\rho}$.
2. The original definition of (ε, r) -reducibility (see [6, Definition 4.4]), is marginally different from the definition above: Instead of $\mathbb{M} \subset L^2_{1/\rho}$, we here require $\mathbb{M} \subset \tilde{\mathbb{M}} \subset L^2_{1/\rho}$. The introduction of this slightly stronger technical requirement allows us to later control a certain embedding error, see Proposition 2.8. Note that the proofs in [6] regarding the optimality of the final reaction coordinate are not affected by this change.

In what follows, we always assume that the process X_t is (ε, r) -reducible with small ε and $r \ll n$.

Remark 2.4. In addition to metastable systems, many other relevant problems possess such transition manifolds. For instance, one can show that, under mild conditions on f and g , systems with explicit time scale separation, given by

$$\begin{aligned} dX_t &= f(X_t, Y_t)dt + dW_t^{(1)}, \\ dY_t &= \frac{1}{\varepsilon}g(X_t, Y_t)dt + \frac{1}{\sqrt{\varepsilon}}dW_t^{(2)}, \end{aligned}$$

also possess a transition manifold since $p_{(x_0, y_0)}^t$ essentially depends only on x_0 for $0 < \varepsilon \ll 1$ and $t \gg \varepsilon$.

2.2. A measure for the quality of reaction coordinates

We will now derive a measure for evaluating the quality of reaction coordinates that is based on transfer operators. The Perron–Frobenius operator $\mathcal{P}^t: L^1(\mathbb{X}) \rightarrow L^1(\mathbb{X})$ associated with the process X_t is defined by

$$(\mathcal{P}^t u)(y) = \int_{\mathbb{X}} u(x) p_x^t(y) dx.$$

This operator can be seen as the push-forward of arbitrary starting densities, i.e., if $X_0 \sim u$, then $X_t \sim \mathcal{P}^t u$.

The operator \mathcal{P}^t can be naturally extended to the inner product space $L^2_{1/\rho}$ and then has particularly advantageous properties (see [2, 37, 26]): Defined on $L^2_{1/\rho}$, the operator \mathcal{P}^t is self-adjoint due to the reversibility of X_t . Moreover, under relatively mild conditions, it does not exhibit any essential spectrum [41]. Hence, its eigenfunctions form an orthonormal basis of $L^2_{1/\rho}$ and the associated eigenvalues are real. Now, the significance of the dominant eigenpairs for the system’s time scales is well-known [41]. This is the primary reason for the choice of the $L^2_{1/\rho}$ -norm in Definition 2.3.

Let θ_i^t be the eigenvalues of \mathcal{P}^t , sorted by decreasing absolute value, and ψ_i the corresponding eigenfunctions, where $i = 0, 1, \dots$. It holds that $\theta_0 = 1$ is independent of t , isolated and the sole eigenvalue with absolute value 1. Furthermore, $\psi_0 = \rho$. The subsequent eigenvalues decrease monotonously to zero both for increasing index and time. That is,

$$\lim_{i \rightarrow \infty} |\theta_i^t| = 0 \quad \text{and} \quad \lim_{t \rightarrow \infty} |\theta_i^t| = 0.$$

The associated eigenfunctions ψ_1, ψ_2, \dots can be interpreted as sub-processes of decreasing longevity in the following sense: Let $u \in L^2_{1/\rho}$, with $u = \sum_{i=0}^{\infty} \alpha_i \psi_i$, $\alpha_i \in \mathbb{R}$, then

$$\mathcal{P}^t u = \sum_{i=0}^{\infty} \theta_i^t \alpha_i \psi_i \approx \sum_{i=0}^d \theta_i^t \alpha_i \psi_i$$

since for the lag time $\tau > 0$ as defined above, there exists an index $d \in \mathbb{N}$ such that $|\theta_i^t| \approx 0$ for all $t \geq \tau$ and all $i > d$. Hence, the major part of the information about the long-term density propagation of X_t is encoded in the d dominant eigenpairs.

In addition to the Perron–Frobenius operator for the full process X_t , we can define the Perron–Frobenius operator for the projected process $\xi(X_t)$, denoted by \mathcal{P}_{ξ}^t . Formally, it can be computed by applying the Zwanzig projection operator Π_{ξ} to \mathcal{P}^t , for details see [50]. Assume now that we are interested in reproducing the long-term dynamics of X_t , i.e., the action of \mathcal{P}^t , for t bigger than some fixed lag time τ . A natural requirement for good reaction coordinates then is

$$\mathcal{P}^t u \approx \mathcal{P}_{\xi}^t u \quad (2)$$

for $t \geq \tau$ and all densities u . Therefore, a necessary condition is

$$\Pi_{\xi} \psi_i \approx \psi_i, \quad i = 0, \dots, d.$$

That is, the eigenfunctions ψ_i must be almost constant along the level sets of ξ . For a formal proof of this statement, see [6]. This motivates the following definition:

Definition 2.5. Let (ψ_i, θ_i^t) be the eigenpairs of the Perron–Frobenius operator. Let $\tau > 0$ and $d \in \mathbb{N}$ such that $\theta_i^t \approx 0$ for all $i > d$ and $t \geq \tau$. We call a function $\xi: \mathbb{X} \rightarrow \mathbb{R}^r$ a good reaction coordinate if for all $i = 0, \dots, d$ there exist functions $\tilde{\psi}_i: \mathbb{R}^r \rightarrow \mathbb{R}$ such that

$$\|\psi_i - \tilde{\psi}_i \circ \xi\|_{\infty} \approx 0. \quad (3)$$

If condition (3) is fulfilled, we say that ξ (approximately) parametrizes the dominant eigenfunctions.

2.3. Optimal reaction coordinates

We now justify why reaction coordinates that are based on parametrizations of the transition manifold \mathbb{M} indeed fulfill the optimality condition (3). Let $Q: L^2_{1/\rho} \rightarrow L^2_{1/\rho}$ be the nearest-point projection onto \mathbb{M} , i.e.,

$$Q(f) = \arg \min_{g \in \mathbb{M}} \|f - g\|_{L^2_{1/\rho}}.$$

Assume further that some parametrization $\gamma: \mathbb{M} \rightarrow \mathbb{R}^r$ of \mathbb{M} is known, i.e., γ is one-to-one on \mathbb{M} and its image in \mathbb{R}^r . The reaction coordinate $\xi: \mathbb{R}^n \rightarrow \mathbb{R}^k$ defined by

$$\xi(x) = (\gamma \circ Q)(p_x^{\tau}) \quad (4)$$

is good in the sense of Definition 2.5.

Theorem 2.6 ([6, Corollary 3.8]). *Let the system be (ε, r) -reducible and ξ defined as in (4). Then for all $i = 0, \dots, d$, there exist functions $\tilde{\psi}_i: \mathbb{R}^r \rightarrow \mathbb{R}$ such that*

$$\|\psi_i - \tilde{\psi}_i \circ \xi\|_\infty \leq \frac{\varepsilon}{|\theta_i^\tau|}. \quad (5)$$

Let us add two remarks:

1. The choice of the $L^2_{1/\rho}$ -norm in Definition 2.3 is crucial for Theorem 2.6 to hold.
2. Metastable systems typically exhibit a time scale gap. Therefore, τ can always be chosen such that $|\theta_i^\tau| \gg 0$, $i = 0, \dots, d$. Consequently, the RC (4) is indeed good according to Definition 2.5.

The main task for the rest of the paper is now the numerical computation of an (approximate) parametrization γ of \mathbb{M} .

2.4. Whitney embedding of the transition manifold

One approach to find a parametrization of \mathbb{M} , proposed by the authors in [6], is to first embed \mathbb{M} into a more accessible Euclidean space and to parametrize the embedded manifold. In order to later compare it with our new method, we will briefly describe this approach here.

To construct an embedding \mathcal{E} that preserves the topological structure of \mathbb{M} , without prior knowledge about \mathbb{M} , a variant of the Whitney embedding theorem can be used. It extends the classic Whitney theorem to arbitrary Banach spaces and was proven by Hunt and Kaloshin in [23].

Theorem 2.7 (Whitney embedding theorem, [23]). *Let \mathbb{V} be a Banach space, let $\mathbb{K} \subset \mathbb{V}$ be a smooth manifold of dimension r and let $k > 2r$. Then almost every (in the sense of prevalence) bounded linear map $\mathcal{F}: \mathbb{V} \rightarrow \mathbb{R}^k$ is one-to-one on \mathbb{K} and its image in \mathbb{R}^k .*

In our case, $\mathbb{V} = L^2_{1/\rho}$ and $\mathbb{K} = \mathbb{M}$ is the transition manifold. Assuming that the dimension r of the transition manifold is known in advance, this result states that we can effectively choose the embedding $\mathcal{F}: L^2_{1/\rho} \rightarrow \mathbb{R}^k$ randomly, and the image $\mathcal{F}(\mathbb{M})$ will again be an r -dimensional manifold in \mathbb{R}^k , provided that $k > 2r$.

We restrict ourselves to embeddings $\mathcal{F}: L^2_{1/\rho} \rightarrow \mathbb{R}^{2r+1}$ of the form

$$\mathcal{F}(f) := \int \eta(x') f(x') dx',$$

with arbitrarily chosen *feature maps* $\eta_i: \mathbb{X} \rightarrow \mathbb{R}$ that we require to be bounded on \mathbb{X} . The *dynamical embedding* of a point $x \in \mathbb{X}$ is then defined by

$$\mathcal{E}(x) := \mathcal{F}(p_x^t) = \int \eta(x') p_x^t(x') dx'. \quad (6)$$

This is the Euclidean representation of the density p_x^t , and the set $\{\mathcal{E}(x) \mid x \in \mathbb{X}\} \subset \mathbb{R}^k$ is the Euclidean representation of the fuzzy transition manifold. It again clusters around an r -dimensional manifold in \mathbb{R}^{2r+1} , namely the image $\mathcal{F}(\mathbb{M})$ of the transition manifold under \mathcal{F} :

Proposition 2.8. *Let the process X_t be (ε, r) -reducible with transition manifold \mathbb{M} , and $\mathcal{F}: L^2_{1/\rho} \rightarrow \mathbb{R}^{2r+1}$ and $\mathcal{E}: \mathbb{R}^n \rightarrow \mathbb{R}^{2r+1}$ defined as above. Then*

$$\inf_{v \in \mathcal{F}(\mathbb{M})} \|v - \mathcal{E}(x)\|_\infty \leq \|\eta\|_\infty \varepsilon \quad \text{for all } x \in \mathbb{X}.$$

Proof. Let $x \in \mathbb{X}$. Then there is an $x^* \in \mathbb{X}$ such that $\|p_x^t - p_{x^*}^t\|_{L^2_{1/\rho}} \leq \varepsilon$. As $\mathbb{M} \subset \tilde{\mathbb{M}}$, i.e., \mathbb{M} consists of transition densities, we have

$$\begin{aligned} \inf_{v \in \mathcal{F}(\mathbb{M})} \|v - \mathcal{E}(x)\|_\infty &\leq \|\mathcal{F}(p_{x^*}^t) - \mathcal{F}(p_x^t)\|_\infty \\ &= \left\| \int_{\mathbb{X}} \eta(x') (p_{x^*}^t(x') - p_x^t(x')) dx' \right\|_\infty \\ &\leq \|\eta\|_\infty \underbrace{\|p_{x^*}^t - p_x^t\|_{L^1}}_{\leq \|p_{x^*}^t - p_x^t\|_{L^2_{1/\rho}}} \leq \|\eta\|_\infty \varepsilon. \end{aligned} \quad \square$$

Remark 2.9. Together, Theorem 2.7 and Proposition 2.8 guarantee at least a minimal degree of well-posedness of the embedding problem: The embedded manifold $\mathcal{F}(\mathbb{M})$ has the same topological structure as \mathbb{M} , and $\mathcal{F}(\tilde{\mathbb{M}})$ clusters closely around it (if $\|\eta\|_\infty$ is small). However, guarantees on the *condition* of the problem cannot be made. The manifold \mathbb{M} will in general be distorted by \mathcal{F} , to a degree that might pose problems for numerical manifold learning algorithms. This problem is illustrated in Figure 2. Such a situation typically occurs if some of the components of the embedding \mathcal{F} are strongly correlated.

Additionally, the Whitney embedding theorem cannot guarantee that the *fuzzy* transition manifold $\tilde{\mathbb{M}}$ will be preserved under the embedding, as analytically $\tilde{\mathbb{M}}$ is not a manifold. Thus, \mathcal{F} is in general not injective on $\tilde{\mathbb{M}}$.

2.5. Data-driven algorithm for parametrizing the transition manifold

Due to its implicit definition, the transition manifold \mathbb{M} is hard to analyze and parametrize without further knowledge of the system. However, as $\mathbb{M} \subset \tilde{\mathbb{M}}$ and $\tilde{\mathbb{M}}$ concentrates ε -closely around \mathbb{M} , we can assume that any parametrization of the dominant directions of $\tilde{\mathbb{M}}$ is also a good parametrization of \mathbb{M} . The embedding $\mathcal{F}(\tilde{\mathbb{M}})$ can be efficiently sampled from simulation data in the following way: Let $X_\tau(x_0, \omega)$ denote the endpoint of the time- τ realization of X_t starting in $x_0 \in \mathbb{X}$ and outcome $\omega \in \Omega$, where Ω is the sample space underlying the process X_t . For $x \in \mathbb{X}$, $\tau > 0$ fixed as in Definition 2.3 and arbitrarily chosen $\{\omega_1, \dots, \omega_M\} \subset \Omega$, let $y^{(k)} := X_\tau(x, \omega_k)$. In practice, the $y^{(k)}$ will be generated by multiple runs of a numerical SDE solver starting in x with M different random seeds.

The *empirical dynamical embedding* $\hat{\mathcal{E}}: \mathbb{R}^n \rightarrow \mathbb{R}^r$ is defined by

$$\hat{\mathcal{E}}(x) := \frac{1}{M} \sum_{k=1}^M \eta(y^{(k)}), \quad (7)$$

and is an estimator for \mathcal{E} .

Let $\mathbb{X}_N = \{x_1, \dots, x_N\}$ be a finite sample of state space points, which covers the “dynamically relevant” part of state space, i.e., the regions of \mathbb{X} of substantial measure ρ . The exact distribution of the sampling points is not important here. If \mathbb{X} is bounded or periodic, \mathbb{X}_N could be drawn from the uniform distribution or chosen to form a regular grid. In practice,

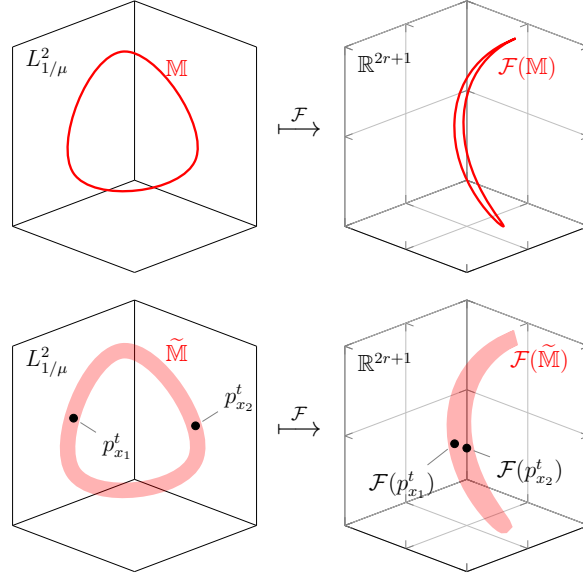


Figure 2: Illustration of the consequences of bad choices for the embedding function. While the topology of the transition manifold \mathbb{M} is preserved under the embedding, the relative distances between its points may be heavily distorted (top row). Intuitively, points that lie on distant parts of the manifold might be mapped closely together. As a consequence, a manifold learning algorithm based on distances between a finite number of samples of $\mathcal{F}(\tilde{\mathbb{M}})$ would have difficulties learning the (in this case circular) topology of \mathbb{M} (bottom row).

it often consists of a sample of the system's equilibrium measure ρ . Due to Proposition 2.8, the point cloud $\hat{\mathcal{E}}(\mathbb{X}_N)$ then clusters around an r -dimensional manifold in \mathbb{R}^k . Parametrizing this manifold is a classical manifold learning task for which a wide variety of algorithms can be deployed. Algorithm 2.1 summarizes the overall procedure of computing good reaction coordinates based on parametrizing the embedded fuzzy transition manifold.

Algorithm 2.1 Whitney embedding based computation of the reaction coordinate.

Input: Transition manifold dimension r , intermediate lag time τ .

- 1: Choose test points $\mathbb{X}_N = \{x_1, \dots, x_N\}$ that cover the relevant parts of state space.
- 2: Randomly choose $2r + 1$ bounded observables $\eta_i: \mathbb{R}^d \rightarrow \mathbb{R}$.
- 3: For each x_i , simulate M independent trajectories of length τ . Let the end points be denoted by $y_i^{(j)}$.
- 4: Compute the embedded empirical densities as $z_i \leftarrow \frac{1}{M} \sum_{j=1}^M \eta(y_i^{(j)}) \in \mathbb{R}^{2r+1}$.
- 5: Compute the distance matrix $D \in \mathbb{R}^{N \times N}$ with $D_{ij} = \|z_i - z_j\|_2$, where $\|\cdot\|_2$ is the Euclidean norm in \mathbb{R}^{2r+1} .
- 6: Apply a distance-based manifold learning algorithm to D . Define $\tilde{\gamma}(z_i) \in \mathbb{R}^r$ to be the resulting parametrization of the embedded points.

Output: An r -dimensional reaction coordinate evaluated at the test points:

$$\xi(x_i) := \tilde{\gamma}(z_i), \quad i = 1, \dots, N.$$

3. Kernel-based parametrization of the transition manifold

The approach described above for learning a parametrization of the transition manifold \mathbb{M} by embedding it into Euclidean spaces requires a priori knowledge of the dimension of \mathbb{M} . Also, more importantly, \mathbb{M} might be strongly distorted by the embedding, as described in Section 2.4. The kernel-based parametrization, which is the main novelty of this work, will address both of these shortcomings by embedding \mathbb{M} into reproducing kernel Hilbert spaces.

3.1. Kernel reformulation of the embedding algorithm

Dimensionality reduction algorithms that can be used in Algorithm 2.1 include Diffusion Maps [14], Multidimensional Scaling [49, 28], and Locally Linear Embedding [36]. These, and many others, require only a notion of distance between pairs of data points. In our case, this amounts to the Euclidean distances between embedded points, i.e., $\|\mathcal{E}(x_i) - \mathcal{E}(x_j)\|_2$, which can be computed by the Euclidean inner products $\langle \mathcal{E}(x_i), \mathcal{E}(x_j) \rangle$, as

$$\|\mathcal{E}(x_i) - \mathcal{E}(x_j)\|_2^2 = \langle \mathcal{E}(x_i), \mathcal{E}(x_i) \rangle - 2\langle \mathcal{E}(x_i), \mathcal{E}(x_j) \rangle + \langle \mathcal{E}(x_j), \mathcal{E}(x_j) \rangle.$$

Other compatible algorithms such as Principal Component Analysis are based directly on the inner products. The inner products can be written as

$$\langle \mathcal{E}(x_i), \mathcal{E}(x_j) \rangle = \iint \langle \eta(y_i), \eta(y_j) \rangle p_{x_i}^t(y_i) p_{x_j}^t(y_j) dy_i dy_j,$$

and the empirical counterpart is

$$\langle \hat{\mathcal{E}}(x_i), \hat{\mathcal{E}}(x_j) \rangle = \frac{1}{M^2} \sum_{l_1, l_2=1}^M \langle \eta(y_i^{(l_1)}), \eta(y_j^{(l_2)}) \rangle.$$

However, rather than *explicitly* computing the inner product between the features on the right-hand side, we now assume that it can be computed *implicitly* by using a *kernel function* $k: \mathbb{X} \times \mathbb{X} \rightarrow \mathbb{R}$, i.e.,

$$k(y_i, y_j) = \langle \eta(y_i), \eta(y_j) \rangle. \quad (8)$$

This assumption, called the *kernel trick*, is commonly used to avoid the costly computation of inner products between high-dimensional features. However, instead of defining the kernel k based on previously chosen features, one typically considers kernels that implicitly define high- and possibly infinite-dimensional feature spaces. In this way, we are able to avoid the choice of feature maps altogether.

Kernels with this property span a so-called *reproducing kernel Hilbert space*:

Definition 3.1 (Reproducing kernel Hilbert space [45]). *Let $k: \mathbb{X} \times \mathbb{X} \rightarrow \mathbb{R}$ be a positive definite function. The set \mathbb{H} of functions $f: \mathbb{X} \rightarrow \mathbb{R}$, together with the corresponding inner product $\langle \cdot, \cdot \rangle_{\mathbb{H}}$ which fulfills*

$$(i) \quad \mathbb{H} = \overline{\text{span}\{k(x, \cdot) \mid x \in \mathbb{X}\}} \text{ and}$$

$$(ii) \quad \langle f, k(x, \cdot) \rangle_{\mathbb{H}} = f(x) \text{ for all } f \in \mathbb{H}$$

is called the reproducing kernel Hilbert space (RKHS) associated with the kernel k .

Requirement (ii) implies that

$$\langle k(x, \cdot), k(x', \cdot) \rangle = k(x, x') \quad \text{for all } x, x' \in \mathbb{X}, \quad (9)$$

thus $\eta(x) := k(x, \cdot)$ can be regarded as a function-valued feature map (the so-called *canonical feature map*). However, each positive definite kernel is guaranteed to also possess a feature map of at most countable dimension.

Theorem 3.2 (Mercer's theorem [32]). *Let k be a positive definite kernel and ν be a finite Borel measure with support \mathbb{X} . Define the integral operator $\mathcal{T}_k: L_\nu^2 \rightarrow L_\nu^2$ by*

$$\mathcal{T}_k f = \int k(\cdot, x) f(x) d\nu(x). \quad (10)$$

Then there is an orthonormal basis $\{\sqrt{\lambda_i} \varphi_i\}$ of \mathbb{H} consisting of eigenfunctions φ_i of \mathcal{T}_k rescaled with the square root of the corresponding nonnegative eigenvalues λ_i such that

$$k(x, x') = \sum_{i=0}^{\infty} \lambda_i \varphi_i(x) \varphi_i(x') \quad \text{for all } x, x' \in \mathbb{X}. \quad (11)$$

The above formulation of Mercer's theorem has been taken from [34]. The *Mercer features* $\eta_i := \sqrt{\lambda_i} \varphi_i$ thus fulfill (8) for their corresponding kernel. In what follows, if not stated otherwise, ν will be the standard Lebesgue measure.

Example 3.3. Examples of commonly used kernels are:

1. Linear kernel: $k(x, x') = x^\top x'$. One sees immediately that (8) is fulfilled by choosing $\eta_i(x) = x_i$, $i = 1, \dots, n$ (also spanning the Mercer feature space).
2. Polynomial kernel of degree p : $k(x, x') = (x^\top x' + 1)^p$. It can be shown that the Mercer feature space is spanned by the monomials in x up to degree p .
3. Gaussian kernel: $k(x, x') = \exp\left(-\frac{1}{\sigma} \|x - x'\|_2^2\right)$, where $\sigma > 0$ is called the *bandwidth* of the kernel. Let $p \in \mathbb{N}$ and $\mathbf{p} = (p_1, \dots, p_n)$ with $p_1 + \dots + p_n = p$ be a multi-index. The Mercer features of k then take the form

$$\eta_{\mathbf{p}}(x) = e_{p_1}(x_1) \cdots e_{p_n}(x_n),$$

see [48], where

$$e_{p_i}(x_i) = \sqrt{\frac{2^{p_i}}{\sigma^{2p_i} p_i!}} x_i^{p_i} \exp\left(-\frac{1}{\sigma^2} x_i^2\right). \quad \triangle$$

Let \mathcal{F}_k denote the density embedding based on the Mercer features of the kernel k , i.e.,

$$(\mathcal{F}_k(p_x^t))_i := \int \eta_i(x') p_x^t(x') dx', \quad i = 0, 1, 2, \dots, \quad (12)$$

and let $\mathcal{E}_k(x) := \mathcal{F}_k(p_x^t)$. The amount of information about p_x^t preserved by the embedding \mathcal{F}_k depends on the choice of the kernel k . For the first two kernels in Example 3.3, the information preserved has a familiar stochastic interpretation (see, e.g., [34, 39, 47]):

1. Let k be the linear kernel. Then

$$\|\mathcal{F}_k(p_{x_1}^t) - \mathcal{F}_k(p_{x_2}^t)\| = 0 \iff \int p_{x_1}^t(y) dy = \int p_{x_2}^t(y) dy,$$

i.e., the means of $p_{x_1}^t$ and $p_{x_2}^t$ coincide.

2. Let k be the polynomial kernel of degree $p > 1$. Then

$$\|\mathcal{F}_k(p_{x_1}^t) - \mathcal{F}_k(p_{x_2}^t)\| = 0 \iff \mathbf{m}_i(p_{x_1}^t) = \mathbf{m}_i(p_{x_2}^t), \quad i = 1, \dots, p,$$

i.e., the first p moments \mathbf{m}_i of $p_{x_1}^t$ and $p_{x_2}^t$ coincide.

Remark 3.4. In practice, comparing the first p moments often is enough to sufficiently distinguish the transition densities that constitute the transition manifold. However, densities that differ only in higher moments cannot be distinguished by \mathcal{F}_k , which means that for the above two kernels, \mathcal{F}_k is not injective. Therefore \mathcal{F}_k does not belong to the prevalent class of maps that is at the heart of the Whitney embedding theorem 2.7. We can therefore not utilize the Whitney embedding theorem to argue that the topology of \mathbb{M} is preserved under \mathcal{F}_k . Instead, in Section 3.2, we will use a different argument to show that the embedding is indeed injective for the Gaussian kernel (and others).

Still, by formally using the Mercer dynamical embedding \mathcal{E}_k in (6) (abusing notation if there are countably infinitely many such features), and using the kernel trick, we can now reformulate Algorithm 2.1 as a *kernel-based* method that does not require the explicit computation of any feature vector. This is summarized in Algorithm 3.1.

Algorithm 3.1 Kernel-based computation of the reaction coordinate.

Input: Kernel $k: \mathbb{X} \times \mathbb{X} \rightarrow \mathbb{R}$, intermediate lag time τ .

- 1: Choose test points $\mathbb{X}_N = \{x_1, \dots, x_N\}$ that cover the relevant parts of state space.
- 2: For each x_i , simulate M independent trajectories of length τ . Let the end points be denoted by $y_i^{(l)}$.
- 3: Compute the kernel matrix $K \in \mathbb{R}^{N \times N}$:

$$K_{ij} = \frac{1}{M^2} \sum_{l_1, l_2=1}^M k(y_i^{(l_1)}, y_j^{(l_2)}).$$

- 4: Compute the distance matrix $D \in \mathbb{R}^{N \times N}$:

$$D_{ij} = K_{ii} + K_{jj} - 2K_{ij}.$$

- 5: Apply a distance-based manifold learning algorithm to the distance matrix D . Denote the resulting parametrization of the underlying i -th element by $\tilde{\gamma}_i \in \mathbb{R}^r$.

Output: An r -dimensional reaction coordinate evaluated at the test points:

$$\xi(x_i) := \tilde{\gamma}_i, \quad i = 1, \dots, N.$$

3.2. Condition of the kernel embedding

We will now investigate to what extent the kernel embedding preserves the topology and geometry of the transition manifold.

3.2.1. Kernel mean embedding

We derived the kernel-based algorithm by considering the embedding \mathcal{F}_k of the transition manifold into the image space of the Mercer features in order to highlight the similarity to the Whitey embedding based on randomly drawn features. Of course, the Mercer features never had to be computed explicitly.

However, in order to investigate the quality of this embedding procedure it is advantageous to consider a different, yet equivalent embedding map: The transition manifold can be directly embedded into the RKHS by means of the *kernel mean embedding* operator.

Definition 3.5. Let k be a positive definite kernel and \mathbb{H} the associated RKHS. Let p be a probability density over \mathbb{X} . Define the kernel mean embedding of p by

$$\mu(p) := \int_{\mathbb{X}} k(x, \cdot) p(x) dx$$

and the empirical kernel mean embedding by

$$\hat{\mu}(p) := \frac{1}{m} \sum_i k(x_i, \cdot) \quad \text{with} \quad \{x_1, \dots, x_m\} \sim p.$$

Note that $\mu(p)$ and $\hat{\mu}(p)$ are again elements of \mathbb{H} and that for ν in (10) being the Lebesgue measure we obtain $\mu(p) = \mathcal{T}_k p$. Further, one sees that

$$\langle \mathcal{F}_k(p_{x_1}^t), \mathcal{F}_k(p_{x_2}^t) \rangle = \langle \mu(p_{x_1}^t), \mu(p_{x_2}^t) \rangle_{\mathbb{H}}.$$

Thus, for investigating whether the embedding \mathcal{F}_k preserves distances or inner products between densities, we can equivalently investigate the embedding μ . This is advantageous as injectivity and isometry properties of the kernel mean embedding are well-studied.

3.2.2. Injectivity of the kernel mean embedding

A first important result is that k can be chosen such that μ is injective. Such kernels are called *characteristic* [21]. In [47], several conditions for characteristic kernels are listed, including the following:

Theorem 3.6 ([47, Theorem 7]). The kernel k is characteristic if for all $f \in L_2$ it holds that

$$\int_{\mathbb{X}} \int_{\mathbb{X}} k(x, x') f(x) f(x') dx dx' > 0. \quad (13)$$

Condition (13) is known as the *Mercer condition*, which is, for example, fulfilled by the Gaussian kernel from Example 3.3. The Mercer features of such a kernel are particularly rich.

Theorem 3.7. Assume that the kernel satisfies the Mercer condition (13). Then the eigenfunctions $\{\psi_i\}$ of \mathcal{T}_k form an orthonormal basis of $L^2(\nu)$.

For more details, see, e.g., [38, 48]. It is easy to see that for kernels fulfilling (13), μ as a map from L^2 to \mathbb{H} is Lipschitz continuous:

Lemma 3.8. Let k be a characteristic kernel with Mercer eigenvalues λ_i , $i \in \mathbb{N}_0$. Then $\mu: L^2 \rightarrow \mathbb{H}$ is Lipschitz continuous with constant

$$c := \sqrt{\lambda_0}. \quad (14)$$

Proof. As μ is linear, it suffices to show that $\|\mu(f)\|_{\mathbb{H}} \leq c\|f\|_2$ for all $f \in L_2$. We obtain

$$\begin{aligned}\|\mu(f)\|_{\mathbb{H}}^2 &= \langle \mu(f), \mu(f) \rangle_{\mathbb{H}} \\ &= \left\langle \int_{\mathbb{X}} f(x)k(x, \cdot)dx, \int_{\mathbb{X}} f(x)k(x, \cdot)dx \right\rangle_{\mathbb{H}} \\ &= \int_{\mathbb{X}} \int_{\mathbb{X}} f(x)f(y)k(x, y)dx dy,\end{aligned}$$

where (9) was used in the last line. By expanding k into its Mercer features via (11), this becomes

$$\begin{aligned}\|\mu(f)\|_{\mathbb{H}}^2 &= \int_{\mathbb{X}} \int_{\mathbb{X}} f(x)f(y) \left(\sum_{i \in \mathbb{N}} \lambda_i \varphi_i(x) \varphi_i(y) \right) dx dy \\ &= \sum_{i \in \mathbb{N}} \lambda_i \langle f, \varphi_i \rangle_{L^2}^2.\end{aligned}$$

By Theorem 3.7, the φ_i form an orthonormal basis of L^2 , and thus

$$\|\mu(f)\|_{\mathbb{H}}^2 \leq \lambda_0 \|f\|_{L^2}^2. \quad \square$$

Thus, if the kernel is characteristic, the structure of the TM and the fuzzy TM are qualitatively preserved under the embedding.

Corollary 3.9. *Let k be a characteristic kernel and let X_t be (ε, r) -reducible. Then $\mu(\mathbb{M})$ is an r -dimensional manifold in \mathbb{H} , and for all $x \in \mathbb{X}$ it holds that*

$$\inf_{g \in \mu(\mathbb{M})} \|g - \mu(p_x^t)\|_{\mathbb{H}} \leq \sqrt{\lambda_0} \|\sqrt{\rho}\|_{\infty} \varepsilon.$$

Proof. By Lemma 3.8, the map $\mu: L^2 \rightarrow \mathbb{H}$ is continuous (and furthermore injective), and thus $\mu(\mathbb{M})$ is again an r -dimensional manifold. For $x \in \mathbb{X}$, consider now any $f \in L_{1/\rho}^2$ with $\|f - p_x^t\|_{L_{1/\rho}^2} \leq \varepsilon$. For $g := \mu(f)$, we then get

$$\|g - \mu(p_x^t)\|_{\mathbb{H}} = \|\mu(f - p_x^t)\|_{\mathbb{H}}$$

which by Lemma 3.8 is

$$\begin{aligned}&\leq \sqrt{\lambda_0} \|\sqrt{\rho}\|_{\infty} \|f - p_x^t\|_{L_{1/\rho}^2} \\ &\leq \sqrt{\lambda_0} \|\sqrt{\rho}\|_{\infty} \varepsilon.\end{aligned} \quad \square$$

Remark 3.10. This result should be seen as an analogue to Proposition 2.8 for the Whitney-based TM embedding. In short, for characteristic kernels, the injectivity and continuity of μ guarantee that the image of \mathbb{M} under μ is again an r -dimensional manifold in \mathbb{H} , and Corollary 3.9 guarantees that the embedded fuzzy transition manifold $\mu(\widehat{\mathbb{M}})$ still clusters closely around $\mu(\mathbb{M})$ (if $\sqrt{\lambda_0}$ and $\|\sqrt{\rho}\|_{\infty}$ in Corollary 3.9 are small). This again guarantees a minimal degree of well-posedness of the problem.

3.2.3. Distortion under the kernel mean embedding

Unlike the Whitney embedding, the kernel embedding now allows us to derive conditions under which the distortion of \mathbb{M} is bounded. We have to show that the $L^2_{1/\rho}$ -distance between points on \mathbb{M} is not overly decreased or increased by the kernel mean embedding. To formalize this, we consider measures for the manifold's internal distortion, following the notions of metric embedding theory [1].

Definition 3.11. *Let μ be the embedding corresponding to a characteristic kernel. The contraction of μ is defined by*

$$\mathcal{C}(\mu) := \sup_{\substack{p, q \in \mathbb{M} \\ q \neq p}} \frac{\|p - q\|_{L^2_{1/\rho}}}{\|\mu(p) - \mu(q)\|_{\mathbb{H}}}. \quad (15)$$

The expansion of μ is defined by

$$\mathcal{E}(\mu) := \sup_{\substack{p, q \in \mathbb{M} \\ q \neq p}} \frac{\|\mu(p) - \mu(q)\|_{\mathbb{H}}}{\|p - q\|_{L^2_{1/\rho}}}. \quad (16)$$

Finally, the distortion of μ is defined by

$$\mathcal{D}(\mu) := \mathcal{C}(\mu)\mathcal{E}(\mu). \quad (17)$$

It follows that $\mathcal{D}(\mu) \geq 1$ and $\mathcal{D}(\mu) = 1$ if and only if μ is isometric. We call the embedding *well-conditioned* if $\mathcal{D}(\mu)$ is small.

Proposition 3.12. *Assume $d_1 > 0$ is the largest and $d_2 > 0$ the smallest bound such that*

$$d_1 \|p - q\|_{L^2_{1/\rho}} \leq \|\mu(p) - \mu(q)\|_{\mathbb{H}} \leq d_2 \|p - q\|_{L^2_{1/\rho}} \quad (18)$$

holds for all $p, q \in \mathbb{M}$. Then the distortion of the kernel embedding is $\mathcal{D}(\mu) = \frac{d_2}{d_1}$.

Proof. Due to the first inequality in (18),

$$\frac{\|p - q\|_{L^2_{1/\rho}}}{\|\mu(p) - \mu(q)\|_{\mathbb{H}}} \leq d_1^{-1} \quad \text{for all } p, q \in \mathbb{M},$$

and thus $\mathcal{C}(\mu) = d_1^{-1}$. Due to the second inequality in (18),

$$\frac{\|\mu(p) - \mu(q)\|_{\mathbb{H}}}{\|p - q\|_{L^2_{1/\rho}}} \leq d_2 \quad \text{for all } p, q \in \mathbb{M},$$

and thus $\mathcal{E}(\mu) = d_2$. Combined, we obtain $\mathcal{D}(\mu) = \frac{d_2}{d_1}$. \square

The second inequality in (18) is just Lipschitz continuity of μ , for which conditions have been derived in Lemma 3.8, so it can be assumed to hold with the corresponding Lipschitz constant.

However, one can show that, even for characteristic kernels, it is not possible to derive a bound d_1 for the first inequality that holds uniformly for all $p, q \in L^2_{1/\rho}$:

Proposition 3.13. *Assume the kernel embedding operator μ has absolutely bounded orthonormal eigenfunctions φ_i with corresponding nonnegative eigenvalues λ_i (arranged in nonincreasing order). Assume λ_i^{-1} increases super-linearly with i . Then there exist functions $p, q \in L^2_{1/\rho}$ such that*

$$\frac{\|\mu(p) - \mu(q)\|_{\mathbb{H}}}{\|p - q\|_{L^2_{1/\rho}}} < \varepsilon$$

for any arbitrarily small $\varepsilon > 0$.

Proof. See Appendix A. □

A similar, but non-quantitative result has been derived in [47, Theorem 19]. The idea behind the proof is that, if p and q vary only in higher eigenfunctions φ_i of the embedding operator μ (see also Theorem 3.2), the \mathbb{H} -distance can become arbitrarily small. If, however, we can reasonably restrict our considerations to the subclass of functions whose variation in the higher φ_i is small compared to the variation in the lower φ_i , a favorable bound d_1 can be derived. Let the expansion of $h = p - q$ be given by

$$h = \sum_{i=0}^{\infty} \tilde{h}_i \varphi_i$$

with the sequence $(\tilde{h}_0, \tilde{h}_1, \dots) \in \ell^2$. Now, for any $i_{\max} \in \mathbb{N}$ such that there exists an index $i \leq i_{\max}$ such that $\tilde{h}_i \neq 0$, define the factor

$$c(h, i_{\max}) := 1 + \frac{\sum_{i=i_{\max}+1}^{\infty} \tilde{h}_i^2}{\sum_{i=0}^{i_{\max}} \tilde{h}_i^2}. \quad (19)$$

This factor bounds the contribution of the higher Mercer eigenfunctions to h by the contribution of the lower ones:

$$\sum_{i=0}^{\infty} \tilde{h}_i^2 = c(h, i_{\max}) \cdot \sum_{i=0}^{i_{\max}} \tilde{h}_i^2.$$

Thus, for an individual h , we can bound the distortion of the L^2 -norm under μ with the help of $c(h, i_{\max})$.

Lemma 3.14. *Let $h \in L^2$, $i_{\max} \in \mathbb{N}$, and $c(h, i_{\max})$ be defined as in (19). Then*

$$\|\mu(h)\|_{\mathbb{H}} \geq \sqrt{\frac{\lambda_{i_{\max}}}{c(h, i_{\max})}} \|h\|_2.$$

Proof. See Appendix A. □

This already shows that for $p, q \in L^2$,

$$\|\mu(p) - \mu(q)\|_{\mathbb{H}} \geq \sqrt{\frac{\lambda_{i_{\max}}}{c(p - q, i_{\max})}} \|p - q\|_{L^2}.$$

However, this is only an intermediate result, as the relevant distance measure in Definition 2.5 is the $L^2_{1/\rho}$ -norm, for reasons detailed in Section 2.2. Unfortunately, a naive estimation yields

$$\|h\|_{L^2_{1/\rho}} \leq \|1/\sqrt{\rho}\|_{\infty} \|h\|_{L^2}. \quad (20)$$

While due to ergodicity $1/\sqrt{\rho}$ is indeed defined on \mathbb{X} , it becomes large in regions of small invariant measure ρ , i.e., “dynamically irrelevant” regions. This would lead to a very small factor d_1 in (18), and thus large predicted distortion. For general h , a more favorable estimate is difficult to obtain. In practice, however, these “dynamically irrelevant” regions are almost never visited by the system such that any practically relevant bound would not suffer from this problem.

Recall that our task is to parametrize the embedded transition manifold, in order to find a parametrization of the dominant transfer operator eigenfunctions ψ_i , $i = 0, \dots, d$. Therefore, differences of p and q in higher eigenfunctions ψ_i , $i > d$, do not need to be resolved. Thus, we only need to preserve the distance

$$\|\Pi_{\text{span}\{\psi_0, \dots, \psi_d\}}(p - q)\|_{L^2_{1/\rho}},$$

where $\Pi_{\text{span}\{\psi_0, \dots, \psi_d\}}$ is the L^2 -orthogonal projection onto the dominant eigenfunctions:

$$\Pi_{\text{span}\{\psi_0, \dots, \psi_d\}}h = \sum_{i=1}^d \langle h, \psi_i \rangle \psi_i.$$

This allows us to derive a more favorable bound:

Lemma 3.15. *Let ψ_i denote the i -th dominant eigenfunction of the Perron–Frobenius operator \mathcal{P}^t and θ_i^t the associated eigenvalues. Let $\Pi_{\text{span}\{\psi_1, \dots, \psi_d\}}: L^2_{1/\rho} \rightarrow L^2_{1/\rho}$ denote the $L^2_{1/\rho}$ -orthogonal projection onto the d dominant eigenfunctions. Then for any $x_1, x_2 \in \mathbb{X}$,*

$$\|\Pi_{\text{span}\{\psi_0, \dots, \psi_d\}}(p_{x_1}^t - p_{x_2}^t)\|_{L^2_{1/\rho}} \leq \sqrt{2d} \sup_{i=0, \dots, d} \|\psi_i/\rho\|_{\infty} |\mathbb{X}| \|\Pi_{\text{span}\{\psi_0, \dots, \psi_d\}}(p_{x_1}^t - p_{x_2}^t)\|_{L^2},$$

where $|\mathbb{X}|$ denotes the Lebesgue measure of \mathbb{X} .

Proof. See Appendix A. □

Remark 3.16. Note that unlike $\|1/\rho\|$ in (20), the factor $\|\psi_i/\rho\|_{\infty}$ is not problematic here, as the dominant eigenfunctions are small whenever ρ is small.

Combining Lemma 3.14 and Lemma 3.15 then finally yields the desired contraction bound:

Corollary 3.17. *Assume there exists $i_{\max} \in \mathbb{N}$ and a constant $c_{\mathbb{X}}(i_{\max}) \geq 1$ such that*

$$c(p_{x_1}^t - p_{x_2}^t, i_{\max}) \leq c_{\mathbb{X}}(i_{\max})$$

for all $x_1, x_2 \in \mathbb{X}$. Then

$$\|\mu(\Pi_{\text{span}\{\psi_1, \dots, \psi_d\}}(p_{x_1}^t - p_{x_2}^t))\|_{\mathbb{H}} \geq d_1 \|\Pi_{\text{span}\{\psi_1, \dots, \psi_d\}}(p_{x_1}^t - p_{x_2}^t)\|_{L^2_{1/\rho}},$$

where $d_1 := \sqrt{\frac{\lambda_{i_{\max}}}{c_{\mathbb{M}}(i_{\max})}} \left(\sqrt{2d} \sup_{i=1, \dots, d} \|\psi_i/\rho\|_{\infty} |\mathbb{X}| \right)^{-1}$.

Remark 3.18. In summary it can be said that, if we can assume that the differences of all p_x^t , $x \in \mathbb{X}$, in the higher Mercer eigenfunctions of μ are uniformly bounded by the differences in the lower Mercer eigenfunctions, then the first inequality in (18) is fulfilled with the above

constant d_1 . Combined with the Lipschitz constant $d_2 = c$ in (14), we have therefore derived an upper bound for the distortion factor of $\mu \circ \Pi_{\text{span}\{\psi_1, \dots, \psi_d\}}$:

$$\mathcal{D}(\mu \circ \Pi_{\text{span}\{\psi_1, \dots, \psi_d\}}) \leq \sqrt{2d\lambda_0 \frac{c_{\mathbb{X}}(i_{\max})}{\lambda_{i_{\max}}}} \sup_{i=1, \dots, d} \|\psi_i / \rho\|_{\infty} |\mathbb{X}|. \quad (21)$$

Most importantly, this bound guarantees the well-posedness of the embedding and parametrization problem as the distortion of even the fuzzy transition manifold cannot become arbitrarily large. We will support this statement with numerical evidence (see Section 4.2) showing that the distortion is, in practice, indeed small. Note, however, that we do not expect (21) to perform well as a quantitative error estimate, as many of the estimates that led to it are rather rough.

4. Illustrative examples and applications

4.1. Reaction coordinate of the Müller–Brown potential

As a first illustrating example, we compute the reaction coordinate of the two-dimensional Müller–Brown potential [33] via the new kernel-based Algorithm 3.1. The potential energy surface (see Figure 3 (a)) possesses three local minima, where the two bottom minima are separated only by a rather shallow energy barrier. Correspondingly, the system’s characteristic long-term behavior is determined by the rare transitions between the minima. These transitions happen predominantly along the potential’s *minimum energy pathway* (MEP), which is shown as white dashed line and was computed using the zero temperature string method [15, 16].

For two sets $A, B \subset \mathbb{X}$ and a starting point $x \in \mathbb{X}$, the *committor function* $q_{AB}(x)$ is defined as the probability that the process hits set A before hitting set B , provided it started in x at time zero. For a precise definition see [41]. For the Müller–Brown potential, the committor function associated with the top left and bottom right energy minima, shown in Figure 3 (b), can be considered an optimal reaction coordinate [18]. Therefore, we use the (qualitative) comparison with the committor function as a benchmark for our reaction coordinate. Note that the computation of the committor function requires global knowledge of the metastable sets and is often not a practical option for the identification of reaction coordinates.

The governing dynamics is given by an overdamped Langevin equation (1), which we solve numerically using the Euler–Maruyama scheme. At inverse temperature $\beta = 0.05$, the lag time $\tau = 0.03$ falls between the slow and fast time scales and is thus defined to be the intermediate lag time. The test points $\{x_1, \dots, x_N\}$ required by Algorithm 3.1 are given by a regular 32×32 grid discretization of the domain $[-1.5, 1.5] \times [-0.5, 2.5]$. For the embedding, the Gaussian kernel

$$k(x, x') = \exp\left(-\frac{\|x - x'\|_2^2}{\sigma}\right) \quad (22)$$

with bandwidth $\sigma = 0.1$ is used and for the manifold learning task in Algorithm 3.1, the diffusion maps algorithm with bandwidth parameter 0.1. The reaction coordinate ξ for the test points is shown in Figure 3 (c). We observe remarkable resemblance to the committor function.

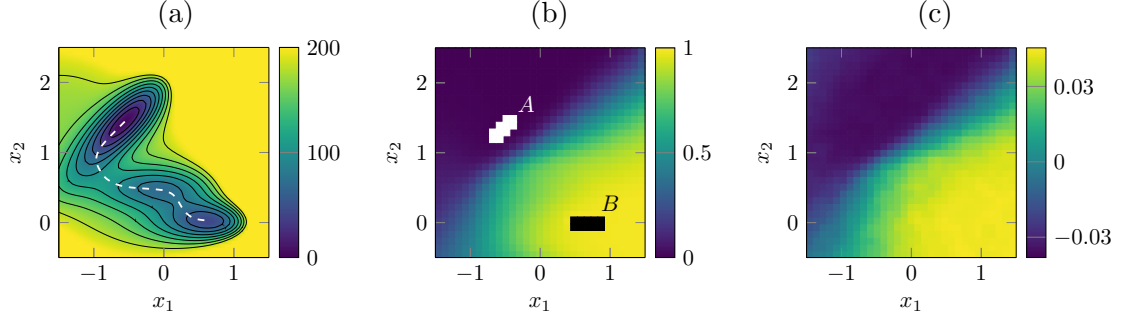


Figure 3: (a) The Müller-Brown potential energy function with its three characteristic local minima and the connecting MEP (white line). (b) The committor function q_{AB} associated with the areas around the top left (A) and bottom right (B) energy minimum. (c) Reaction coordinate ξ of the Müller-Brown potential, computed by Algorithm 3.1.

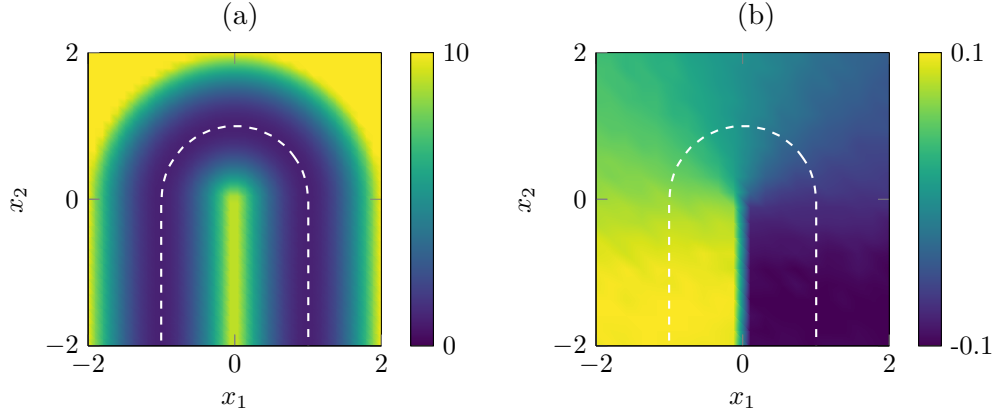


Figure 4: Horseshoe potential. (a) Potential energy function. (b) Reaction coordinate computed with the kernel algorithm. The white dashed line represents the MEP.

4.2. Distortion under the Whitney and kernel embeddings

We now demonstrate the distortion of the transition manifold under the embedding via Algorithm 2.1 (Whitney embedding) and Algorithm 3.1 (kernel-based embedding). To this end, we consider the two-dimensional potential depicted in Figure 4 (a). Good reaction coordinates of a diffusion process in this potential should parametrize the “horseshoe-like” MEP shown as a white dashed line. Such a reaction coordinate is depicted in Figure 4 (b).

As test points x_i , $N = 200$ uniformly distributed random points in the region $\mathbb{X} = [-2, 2]^2$ are drawn. Per point, $M = 100$ short trajectories of length $\tau = 2$ are computed to sample the $p_{x_i}^\tau$.

Whitney embedding

For the Whitney embedding, the expected manifold dimension $r = 1$ is assumed to be known in advance. To demonstrate the different effects of “good” and “bad” embedding functions,

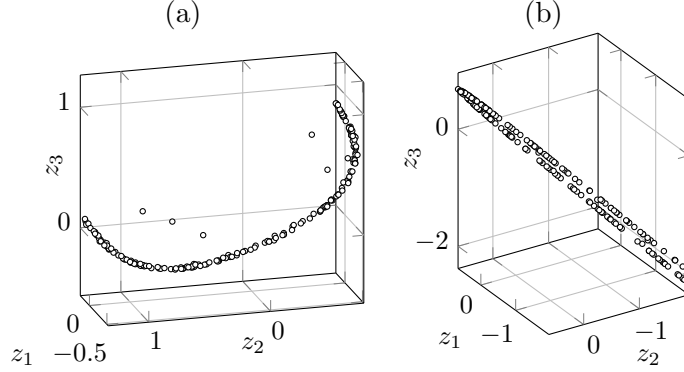


Figure 5: Whitney embeddings of the test points for different observable functions. (a) Pairwise strongly linearly independent coefficient vectors, i.e., “good” observables. (b) Almost pairwise linearly dependent coefficient vectors, i.e., “bad” observables.

two $2r + 1$ -dimensional linear observables $\eta : \mathbb{R}^2 \rightarrow \mathbb{R}^3$ were chosen:

$$\eta_g : x \mapsto A_g x, \quad \eta_b : x \mapsto A_b x, \quad A_g, A_b \in \mathbb{R}^{3 \times 2}.$$

The coefficients of A_g of the “good” embedding function η_g were chosen randomly via the Matlab command

$$\text{rng}(1); \mathbf{A_g} = \text{rand}(3, 2) - 0.5,$$

which produced row vectors that are pairwise strongly linearly independent, i.e., η_a consists of three distinct observable functions. On the other hand, the matrix A_b of the “bad” embedding η_b was constructed to consist of three row vectors that are pairwise almost linearly dependent:

$$A_b = \begin{pmatrix} 0 & 1 \\ \varepsilon & 1 + \varepsilon \\ -\varepsilon & 1 - \varepsilon \end{pmatrix} \quad \text{with } \varepsilon = 0.05.$$

The components of η_b are thus very similar to each other.

The image of the test points under the dynamical embedding \mathcal{E} is shown in Figure 5. On one hand, with the “good” embedding η_a , a curved manifold, corresponding to the curved MEP, is easily discoverable (see Figure 5 (a)) and parametrizable by established manifold learning algorithms. For the “bad” embedding η_b , on the other hand, the distance between opposing points on the MEP is significantly shortened (see Figure 5 (b)), making numerical identification of the manifold structure difficult.

Kernel embedding

For the kernel embedding, we again utilize the Gaussian kernel (22) with bandwidth $\sigma = 10^{-3}$. The result of the kernel embedding of the test points is an approximation of the kernel distance matrix

$$D_{ij} = \|\mu(p_{x_i}^t) - \mu(p_{x_j}^t)\|_{\mathbb{H}}$$

(see Algorithm 3.1), which cannot be visualized directly. We thus apply the Multidimensional scaling (MDS) algorithm to D , in order to visualize the level of similarity between the embedded densities.

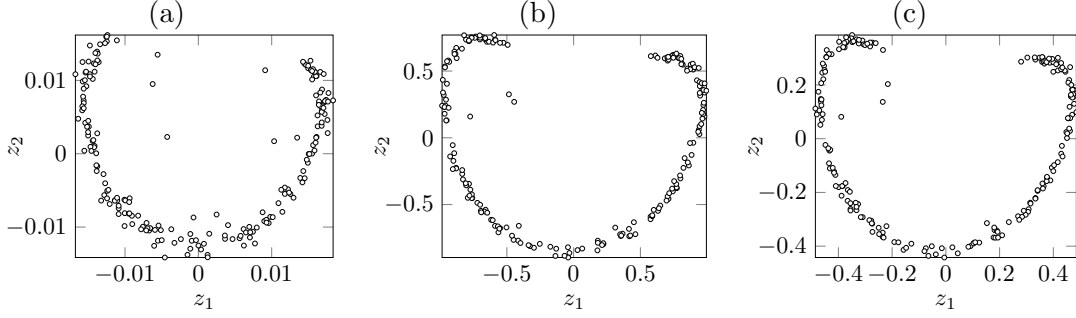


Figure 6: MDS representations of different distance matrices between the transition densities. (a) Kernel distance matrix between embedded transition densities $\mu(p_x^t)$. The point cloud is a representations of the fuzzy transition manifold embedded into \mathbb{H} . (b) $L^2_{1/\rho}$ distance matrix between transition densities p_x^t . (c) L^2 distance matrix between transition densities p_x^t .

Given a distance matrix D , MDS generates points $z_i \in \mathbb{R}^k$ in a Euclidean space of a chosen dimension $k \in \mathbb{N}$ such that the pairwise distance between the z_i corresponds to the distances in D . For an overview of different MDS methods, see for example [49]. We here use the implementation of classical MDS given by the `cmdscale` method in Matlab.

The MDS representation of the kernel distance matrix for $k = 2$ is shown in Figure 6 (a). The curved structure of the MEP is immediately visible. Moreover, it is also possible to visualize the corresponding $L^2_{1/\rho}$ and L^2 distance matrices via MDS, i.e., the matrices

$$(D_{L^2_{1/\rho}})_{ij} := \|p_{x_i}^t - p_{x_j}^t\|_{L^2_{1/\rho}} \quad \text{and} \quad (D_{L^2})_{ij} := \|p_{x_i}^t - p_{x_j}^t\|_{L^2}.$$

The results are shown in Figure 6 (b) & (c).

The MDS representation of D is structurally very similar to $D_{L^2_{1/\rho}}$ and D_{L^2} . This suggests that the $L^2_{1/\rho}$ and L^2 distances are preserved very well under μ , up to a constant factor. To confirm this, we now compute the maximum distortion of the $L^2_{1/\rho}$ metric based on the given test points, i.e., $\mathcal{D}_N(\mu) := \mathcal{C}_N(\mu) \mathcal{E}_N(\mu)$ where

$$\mathcal{C}_N(\mu) := \max_{\substack{i,j=1,\dots,N \\ i \neq j}} \frac{\|p_{x_i}^\tau - p_{x_j}^\tau\|_{L^2_{1/\rho}}}{\|\mu(p_{x_i}^\tau) - \mu(p_{x_j}^\tau)\|_{\mathbb{H}}}, \quad \mathcal{E}_N(\mu) := \max_{\substack{i,j=1,\dots,N \\ i \neq j}} \frac{\|\mu(p_{x_i}^\tau) - \mu(p_{x_j}^\tau)\|_{\mathbb{H}}}{\|p_{x_i}^\tau - p_{x_j}^\tau\|_{L^2_{1/\rho}}}.$$

For large enough N , we expect $\mathcal{D}_N(\mu)$ to be a good estimator for $\mathcal{D}(\mu)$.

The blue graph in Figure 7 shows the dependence of this distortion on the kernel parameter σ . For small enough σ , the distortion $\mathcal{D}_N(\mu)$ is moderately small, with a minimum of $\mathcal{D}_N(\mu) = 36.7$ at $\sigma \approx 10^{-3}$. Compared to the Whitney embeddings, with analogously-defined maximal distortions $\mathcal{D}_N(\mu) \approx 6 \cdot 10^2$ for the “good” embedding η_g , and $\mathcal{D}_N(\mu) \approx 7 \cdot 10^3$ for the “bad” embedding η_b , the kernel embedding can definitely be described as well conditioned.

Remark 4.1. Analogously, we can also define and compute the maximum distortion $\mathcal{D}_N(\mu)$ of the L^2 -metric (red graph in Figure 7). Here, for $\sigma \approx 10^{-1}$ we obtain $\mathcal{D}_N(\mu) = 2.7$, i.e., the embedding becomes nearly isometric. This is not surprising as it has been shown in [47] that for radial kernels $k_\sigma(x, y) = \sigma^{-d} g(\sigma^{-1} \|x - y\|)$ where g is bounded, continuous, and positive definite, it holds that

$$\lim_{\sigma \rightarrow 0} \|\mu_{k_\sigma}(p) - \mu_{k_\sigma}(q)\|_{\mathbb{H}} = \|p - q\|_{L^2}.$$

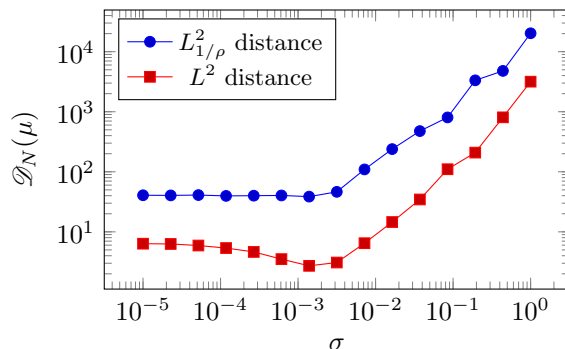


Figure 7: Maximum distortion $\mathcal{D}(\mu)$ of the $L^2_{1/\rho}$ and L^2 distance under the kernel embedding μ for the Gaussian kernel depending on the kernel bandwidth σ .

The Gaussian kernel belongs to this class of kernels. We thus expect that by increasing the sample number M of the transition densities and further decreasing σ , the distortion can be reduced further. However, recall that for our application, only the distortion of the $L^2_{1/\rho}$ distance is relevant.

4.3. Alanine dipeptide

We now demonstrate the applicability of Algorithm 3.1 to realistic, high-dimensional molecular systems by computing reaction coordinates of the Alanine dipeptide. The peptide, depicted in Figure 8 (a), consists of 22 atoms, the state space \mathbb{X} thus has the dimension $n = 66$.

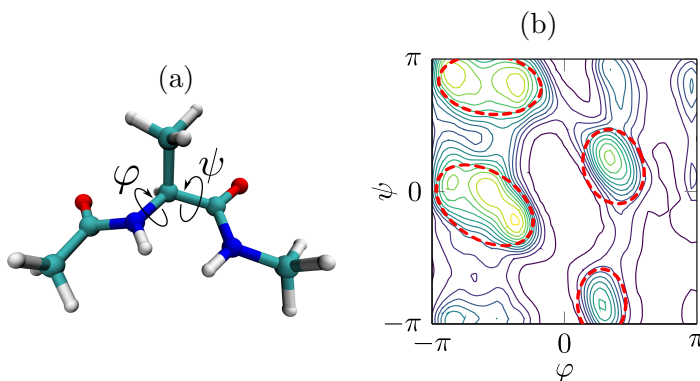


Figure 8: The Alanine dipeptide. (a) Three-dimensional structure with the two essential dihedral angles (φ, ψ) highlighted. (b) The Ramachandran plot of (φ, ψ) reveals four local energy minima, i.e., metastable sets.

It is well-known that the essential long-term behavior of this system is governed by the metastable transitions between four local minima of the potential energy surface (PES) [13, 44]. These minima are clearly visible when projecting the PES onto two specific backbone dihedral angles (φ, ψ) that we call *essential* from now on (see Figure 8 (b)). The transition between the metastable states happens along minimal energy pathways that we aim to reveal with our reaction coordinate. Note however that no information about the existence of the

two essential dihedral angles was used in our experiments, and we perform all of the analysis on the full 66-dimensional data.

The simulations were performed using the Gromacs molecular dynamics software [3]. We consider the molecule in explicit aqueous solution at temperature 400 K (the water molecules are discarded prior to further analysis). To generate the test points x_i , $N = 1000$ snapshots from a long, equilibrated trajectory were subsampled. This guarantees that the x_i cover the dynamically relevant regions of \mathbb{X} , i.e., the metastable sets and transition pathways. The intermediate lag time $\tau = 20$ ps falls between the slow and fast time scales. For strategies to estimate τ prior to simulation, see [5]. For each test point x_i , $M = 100$ simulations of length τ were performed, which took 40 h on a 96 core cluster. The resulting point clouds $\{y_i^{(l)}, l = 1, \dots, M\}$ are samplings of the densities $p_{x_i}^\tau$.

To compute the kernel distance matrix D from the simulation data, the Gaussian kernel (22) with bandwidth $\sigma = 0.1$ was chosen. For the plug-in manifold learning algorithm that is applied to D , the diffusion maps algorithm with bandwidth parameter 0.01 was used. The analysis of the simulation data was performed in Matlab and took 4 minutes on a 4 core laptop.

Figure 9 (a) shows the leading spectrum of the diffusion map matrix that was computed based on D . The first diffusion map eigenvalue is always one, and the associated eigenvector carries no structural information. Therefore, a spectral gap after the third sub-dominant eigenvalue indicates that the underlying transition manifold is intrinsically three-dimensional. The associated three subdominant eigenvectors now are the final reaction coordinate. For each of the 1000 test points, the values of the three eigenvectors are shown in Figure 9 (b). This can be seen as the embedding of the test points into the reaction coordinate space. Here we observe four clusters of points, and three connecting paths. Figure 10, which compares the values of the essential dihedral angles in the test points with the three components of the reaction coordinates, confirms that the four clusters correspond to the metastable sets, and the paths to the transition regions between them.

5. Conclusion and future work

In this work, we have analyzed the embedding of manifolds that lie in certain function spaces into reproducing kernel Hilbert spaces. Moreover, we have proposed efficient numerical algorithms for learning parametrizations of these embedded manifolds from data. The question is motivated by the recent insight that parametrizations of the so-called transition manifold, a manifold consisting of the transition density functions of a stochastic system, are strongly linked to reduced coordinates for that system. The method can thus be used for coarse graining a given system.

Compared to previous approaches based on random embeddings into a Euclidean space, the new kernel-based approach eliminates the need to know the transition manifold dimension a priori. Furthermore, if a universal kernel is used, the topological structure of the transition manifold is guaranteed to be preserved under the embedding. We have derived bounds for the geometric distortion of the transition manifold under the RKHS embedding, which can be interpreted as the condition of the overall coarse graining procedure. Correspondingly, the numerical algorithm was demonstrated to be very robust, especially when compared to random embeddings, and, in realistic applications, we obtained very favorable results regarding algorithmic distortion bounds.

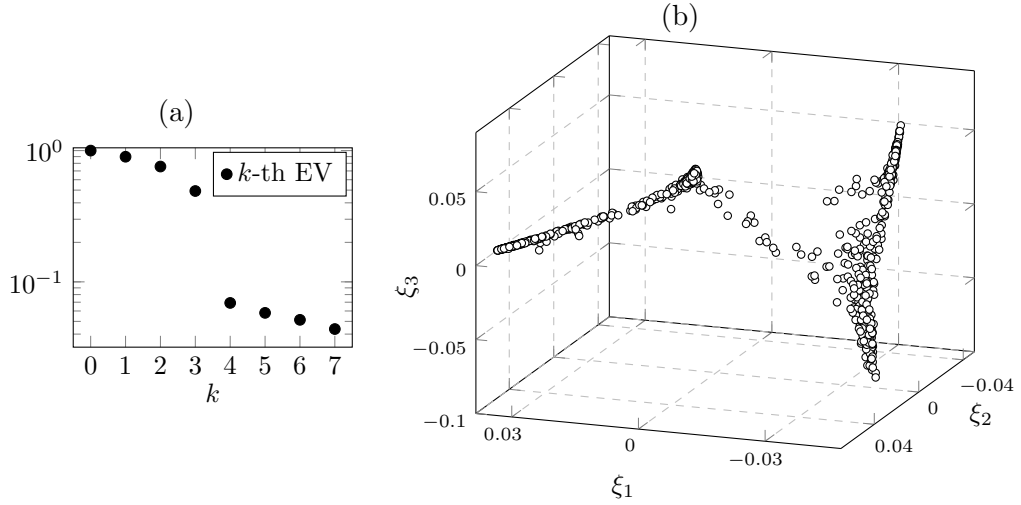


Figure 9: Analysis of the kernel distance matrix D . (a) Eigenvalues of the diffusion map matrix. The existence of three eigenvalues close to 1 (not counting the eigenvalue 1 itself) indicates a three-dimensional reaction coordinate. (b) Test points in the space of the three sub-dominant diffusion map eigenvectors, i.e., the final three-dimensional reaction coordinate.

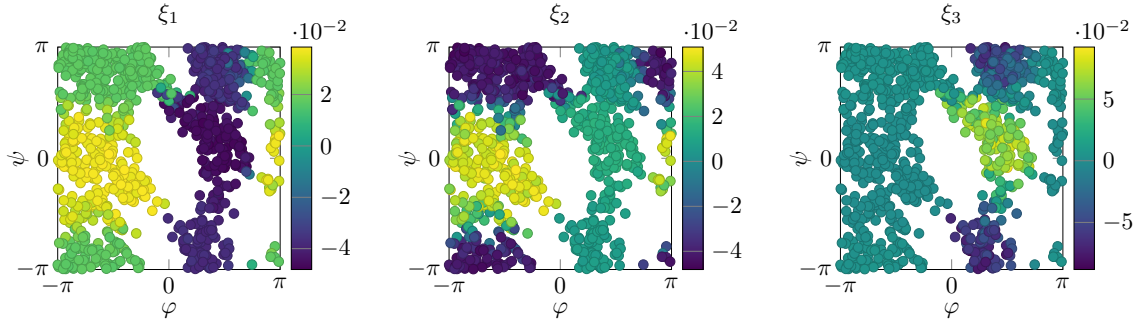


Figure 10: The dihedral angles in the test points, colored by the three components of the reaction coordinate ξ .

There are several new avenues to use the broader theory of kernel embeddings to characterize the kernel embedding of transition manifolds. First, we plan to improve the theoretic distortion bounds derived in Section 3.2 by considering different established interpretations of the metric defined by $d(p, q) = \|\mu(p) - \mu(q)\|_{\mathbb{H}}$. For an overview, see [47].

Recently, the spectral theory of transfer operators was extended to reproducing kernel Hilbert spaces in [27]. The usefulness of this new theory for the data-driven conformation analysis of molecular systems was demonstrated in [25]. As the transition manifold can be defined via the transfer operator², it seems natural to attempt to relate the embedded transition manifold to the kernel transfer operators and corresponding embedded transfer operators defined in [27].

Finally, as illustrated in [7, 8, 9], RKHSs can act as *linearizing spaces* in the sense that

²The fuzzy transition manifold is the image of all Dirac densities under the transfer operator, i.e., $\tilde{\mathbb{M}} = \{\mathcal{T}^t \delta_x \mid x \in \mathbb{X}\}$.

performing linear analysis in the RKHS can capture strong nonlinearities in the original system. A typical example is the problem of linear separability in data classification: A data set which is not linearly separable might be easily separated when mapped into a nonlinear feature space. In our current context, this means that efficient linear manifold learning methods might be suitable to parametrize the embedded manifold, if the kernel is chosen appropriately. We will investigate whether a corresponding theory can be developed.

Acknowledgements

The authors would like to thank Péter Koltai for helpful discussions regarding the distortion analysis of the kernel embedding. This research has been partially funded by Deutsche Forschungsgemeinschaft (DFG) through grant CRC 1114.

References

- [1] I. Abraham, Y. Bartal, and O. Neiman. Advances in metric embedding theory. *Advances in Mathematics*, 228(6):3026 – 3126, 2011.
- [2] J. R. Baxter and J. S. Rosenthal. Rates of convergence for everywhere-positive Markov chains. *Stat. Probab. Lett.*, 22(4):333–338, 1995.
- [3] H. Berendsen, D. van der Spoel, and R. van Drunen. Gromacs: A message-passing parallel molecular dynamics implementation. *Computer Physics Communications*, 91(1):43–56, 1995.
- [4] R. B. Best and G. Hummer. Reaction coordinates and rates from transition paths. *Proceedings of the National Academy of Sciences*, 102(19):6732–6737, 2005.
- [5] A. Bittracher, R. Banisch, and C. Schütte. Data-driven computation of molecular reaction coordinates. *The Journal of Chemical Physics*, 149(15):154103, 2018.
- [6] A. Bittracher, P. Koltai, S. Klus, R. Banisch, M. Dellnitz, and C. Schütte. Transition Manifolds of Complex Metastable Systems: Theory and Data-driven Computation of Effective Dynamics. *Journal of Nonlinear Science*, 28(2):471–512, 2017.
- [7] J. Bouvrie and B. Hamzi. Balanced reduction of nonlinear control systems in reproducing kernel Hilbert space. *Proc. 48th Annual Allerton Conference on Communication, Control, and Computing*, pages 294–301, 2010.
- [8] J. Bouvrie and B. Hamzi. Kernel methods for the approximation of nonlinear systems. *SIAM Journal on Control and Optimization*, 55(4):2460–2492, 2017.
- [9] J. Bouvrie and B. Hamzi. Kernel methods for the approximation of some key quantities of nonlinear systems. *Journal of Computational Dynamics*, 4(1):1–19, 2017.
- [10] G. Bowman, V. Volez, and V. S. Pande. Taming the complexity of protein folding. *Curr. Opin. Struct. Biol.*, 21(1):4–11, 2011.

- [11] G. R. Bowman, V. S. Pande, and F. Noé, editors. *An Introduction to Markov State Models and Their Application to Long Timescale Molecular Simulation*, volume 797 of *Advances in Experimental Medicine and Biology*. Springer, 2014.
- [12] C. J. Camacho and D. Thirumalai. Kinetics and thermodynamics of folding in model proteins. *Proc. Natl. Acad. Sci.*, 90(13):6369–6372, 1993.
- [13] D. S. Chekmarev, T. Ishida, and R. M. Levy. Long-time conformational transitions of alanine dipeptide in aqueous solution: Continuous and discrete-state kinetic models. *The Journal of Physical Chemistry B*, 108(50):19487–19495, 2004.
- [14] R. R. Coifman, I. G. Kevrekidis, S. Lafon, M. Maggioni, and B. Nadler. Diffusion Maps, Reduction Coordinates, and Low Dimensional Representation of Stochastic Systems. *Multiscale Model. Simul.*, 7(2):842–864, 2008.
- [15] W. E, W. Ren, and E. Vanden-Eijnden. String method for the study of rare events. *Phys. Rev. B*, 66:052301, Aug 2002.
- [16] W. E, W. Ren, and E. Vanden-Eijnden. Simplified and improved string method for computing the minimum energy paths in barrier-crossing events. *The Journal of Chemical Physics*, 126(16):164103, 2007.
- [17] W. E and E. Vanden-Eijnden. Towards a Theory of Transition Paths. *J. Stat. Phys.*, 123(3):503–523, 2006.
- [18] R. Elber, J. M. Bello-Rivas, P. Ma, A. E. Cardenas, and A. Fathizadeh. Calculating iso-committor surfaces as optimal reaction coordinates with milestoning. *Entropy*, 19(5), 2017.
- [19] P. L. Freddolino, C. B. Harrison, Y. Liu, and K. Schulten. Challenges in protein folding simulations: Timescale, representation, and analysis. *Nature physics*, 6(10):751, 2010.
- [20] G. Froyland, G. A. Gottwald, and A. Hammerlindl. A trajectory-free framework for analysing multiscale systems. *Phys. D Nonlinear Phenom.*, 328:34–43, 2016.
- [21] K. Fukumizu, A. Gretton, X. Sun, and B. Schölkopf. Kernel measures of conditional dependence. In *Proceedings of the 20th International Conference on Neural Information Processing Systems*, NIPS’07, pages 489–496, USA, 2007. Curran Associates Inc.
- [22] A. Gretton, K. M. Borgwardt, M. J. Rasch, B. Schölkopf, and A. Smola. A kernel two-sample test. *Journal of Machine Learning Research*, 13(Mar):723–773, 2012.
- [23] B. Hunt and V. Kaloshin. Regularity of embeddings of infinite-dimensional fractal sets into finite-dimensional spaces. *Nonlinearity*, 12(5):1263–1275, 1999.
- [24] R. Klein. Scale-dependent models for atmospheric flows. *Annual Review of Fluid Mechanics*, 42(1):249–274, 2010.
- [25] S. Klus, A. Bittracher, I. Schuster, and C. Schütte. A kernel-based approach to molecular conformation analysis. *The Journal of Chemical Physics*, 149(24):244109, 2018.

- [26] S. Klus, F. Nüske, P. Koltai, H. Wu, I. Kevrekidis, C. Schütte, and F. Noé. Data-driven model reduction and transfer operator approximation. *Journal of Nonlinear Science*, 28:985–1010, 2018.
- [27] S. Klus, I. Schuster, and K. Muandet. Eigendecompositions of transfer operators in reproducing kernel Hilbert spaces. *arXiv Preprint*, 2017.
- [28] J. B. Kruskal. Nonmetric multidimensional scaling: A numerical method. *Psychometrika*, 29(2):115–129, jun 1964.
- [29] A. J. Majda and R. Klein. Systematic multiscale models for the tropics. *Journal of the Atmospheric Sciences*, 60(2):393–408, 2003.
- [30] R. T. McGibbon, B. E. Husic, and V. S. Pande. Identification of simple reaction coordinates from complex dynamics. *J. Chem. Phys.*, 146(4):44109, 2017.
- [31] T. Melzer, M. Reiter, and H. Bischof. Nonlinear feature extraction using generalized canonical correlation analysis. In G. Dorffner, H. Bischof, and K. Hornik, editors, *Artificial Neural Networks — ICANN 2001*, pages 353–360. Springer Berlin Heidelberg, 2001.
- [32] J. Mercer. Functions of positive and negative type, and their connection the theory of integral equations. *Philosophical Transactions of the Royal Society of London A: Mathematical, Physical and Engineering Sciences*, 209(441-458):415–446, 1909.
- [33] K. Müller. Reaction paths on multidimensional energy hypersurfaces. *Angewandte Chemie International Edition in English*, 19(1):1–13, 1980.
- [34] K. Muandet, K. Fukumizu, B. Sriperumbudur, and B. Schölkopf. Kernel mean embedding of distributions: A review and beyond. *Foundations and Trends in Machine Learning*, 10(1-2):1–141, 2017.
- [35] F. Noé, C. Schütte, E. Vanden-Eijnden, L. Reich, and T. R. Weikl. Constructing the Full Ensemble of Folding Pathways from Short Off-Equilibrium Simulations. *Proc. Natl. Acad. Sci.*, 106(45):19011–19016, 2009.
- [36] S. T. Roweis and L. K. Saul. Nonlinear dimensionality reduction by locally linear embedding. *science*, 290(5500):2323–2326, 2000.
- [37] M. J. Schervish and B. P. Carlin. On the convergence of successive substitution sampling. *J. Comput. Graph. Stat.*, 1(2):111–127, 1992.
- [38] B. Schölkopf and A. J. Smola. *Learning with kernels: support vector machines, regularization, optimization, and beyond*. MIT press, 2001.
- [39] B. Schölkopf, K. Muandet, K. Fukumizu, S. Harmeling, and J. Peters. Computing functions of random variables via reproducing kernel Hilbert space representations. *Statistics and Computing*, 25(4):755–766, Jul 2015.
- [40] B. Schölkopf, A. Smola, and K.-R. Müller. Nonlinear component analysis as a kernel eigenvalue problem. *Neural Computation*, 10(5):1299–1319, 1998.

- [41] C. Schütte and M. Sarich. *Metastability and Markov State Models in Molecular Dynamics: Modeling, Analysis, Algorithmic Approaches*. Number 24 in Courant Lecture Notes. American Mathematical Society, 2013.
- [42] C. Schütte and M. Sarich. *Metastability and Markov State Models in Molecular Dynamics: Modeling, Analysis, Algorithmic Approaches*. Courant Lecture Notes in Mathematics. American Mathematical Society, 2014.
- [43] C. R. Schwantes and V. S. Pande. Modeling molecular kinetics with tICA and the kernel trick. *Journal of Chemical Theory and Computation*, 11(2):600–608, 2015.
- [44] P. E. Smith. The alanine dipeptide free energy surface in solution. *The Journal of Chemical Physics*, 111(12):5568–5579, 1999.
- [45] A. Smola, A. Gretton, L. Song, and B. Schölkopf. A Hilbert space embedding for distributions. In *Proceedings of the 18th International Conference on Algorithmic Learning Theory*, pages 13–31. Springer-Verlag, 2007.
- [46] N. D. Socci, J. N. Onuchic, and P. G. Wolynes. Diffusive dynamics of the reaction coordinate for protein folding funnels. *J. Chem. Phys.*, 104(15):5860–5868, 1996.
- [47] B. K. Sriperumbudur, A. Gretton, K. Fukumizu, B. Schölkopf, and G. R. Lanckriet. Hilbert space embeddings and metrics on probability measures. *J. Mach. Learn. Res.*, 11:1517–1561, Aug. 2010.
- [48] I. Steinwart and A. Christmann. *Support Vector Machines*. Springer, New York, 1st edition, 2008.
- [49] F. W. Young. *Multidimensional scaling: History, theory, and applications*. Psychology Press, 2013.
- [50] W. Zhang, C. Hartmann, and C. Schütte. Effective dynamics along given reaction coordinates, and reaction rate theory. *Faraday Discuss.*, 195:365–394, 2016.

A. Proof of the distortion bounds

Proof of Proposition 3.13. First, note that $L^2_{1/\rho} \subset L^2$, as for $p \in L^2_{1/\rho}$

$$\|p\|_{L^2} = \|\sqrt{\rho}p\|_{L^2_{1/\rho}} \leq \|\sqrt{\rho}\|_{\infty} \|p\|_{L^2_{1/\rho}}. \quad (23)$$

Let (λ_i, φ_i) be the eigenpairs of the integral operator \mathcal{T}_k , ordered in decreasing order of λ_i . For arbitrary $p \in L^2_{1/\rho}$ consider the decomposition into the basis $\{\varphi_i\}_{i \in \mathbb{N}}$ of L^2 :

$$p = \sum_{i=0}^{\infty} \tilde{p}_i \varphi_i.$$

Select $i_{\max} \in \mathbb{N}$ such that $\lambda_i < (\varepsilon / \|\sqrt{\rho}\|_{\infty})^2$ for all $i \geq i_{\max}$, and define

$$q = \sum_{i=i_{\max}}^{\infty} \tilde{p}_i \varphi_i.$$

Then,

$$\|p - q\|_{L^2}^2 = \left\| \sum_{i=i_{\max}}^{\infty} \tilde{p}_i \varphi_i \right\|_{L^2}^2 = \sum_{i=i_{\max}}^{\infty} \tilde{p}_i^2.$$

Further, using that $\{\sqrt{\lambda_i} \varphi_i\}_{i \in \mathbb{N}}$ forms an orthonormal basis of \mathbb{H} , and that μ is a linear operator, we get

$$\|\mu(p) - \mu(q)\|_{\mathbb{H}}^2 = \left\| \sum_{i=i_{\max}}^{\infty} \tilde{p}_i \lambda_i \varphi_i \right\|_{\mathbb{H}}^2 = \sum_{i=i_{\max}}^{\infty} \lambda_i \tilde{p}_i^2 \leq \lambda_{i_{\max}} \sum_{i=i_{\max}}^{\infty} \tilde{p}_i^2.$$

Thus we get

$$\frac{\|\mu(p) - \mu(q)\|_{\mathbb{H}}}{\|p - q\|_{L^2}} \leq \sqrt{\lambda_{i_{\max}}} < \varepsilon / \|\sqrt{\rho}\|_{\infty},$$

and with (23) finally

$$\frac{\|\mu(p) - \mu(q)\|_{\mathbb{H}}}{\|p - q\|_{L^2_{1/\rho}}} \leq \varepsilon. \quad \square$$

Proof of Lemma 3.14. As $\{\sqrt{\lambda_i} \varphi_i\}_{i \in \mathbb{N}_0}$ forms an orthonormal basis of \mathbb{H} , we obtain

$$\|\mu(h)\|_{\mathbb{H}}^2 = \left\| \sum_{i=0}^{\infty} \tilde{h}_i \lambda_i \varphi_i \right\|_{\mathbb{H}}^2 = \sum_{i=0}^{\infty} \lambda_i \tilde{h}_i^2 \geq \sum_{i=0}^{i_{\max}} \lambda_i \tilde{h}_i^2.$$

Further, $\{\varphi_i\}_{i \in \mathbb{N}_0}$ forms an orthonormal basis of L_2 , and so

$$\|h\|_2^2 = \left\| \sum_{i=0}^{\infty} \tilde{h}_i \varphi_i \right\|_2^2 = \sum_{i=0}^{\infty} \tilde{h}_i^2 = c(h, i_{\max}) \cdot \sum_{i=0}^{i_{\max}} \tilde{h}_i^2.$$

Thus,

$$\frac{\|\mu(h)\|_{\mathbb{H}}}{\|h\|_2} \geq \left(\frac{\sum_{i=0}^{i_{\max}} \lambda_i \tilde{h}_i^2}{c(h, i_{\max}) \cdot \sum_{i=0}^{i_{\max}} \tilde{h}_i^2} \right)^{1/2} \geq \sqrt{\frac{\lambda_{i_{\max}}}{c(h, i_{\max})}}. \quad \square$$

Proof of Lemma 3.15. As mentioned in Section 2, the eigenfunctions ψ_i of the Perron–Frobenius operator \mathcal{P}^t form an orthonormal basis of $L^2_{1/\rho}$. Writing p_x^t in the basis $\{\psi_i\}$ and formally using $p_x^t = \mathcal{P}^t \delta_x$, where δ_x is the Dirac density, gives

$$p_x^t = \sum_{i=0}^{\infty} \theta_i^t \langle \delta_x, \psi_i \rangle_{L^2_{1/\rho}} \psi_i = \sum_{i=0}^{\infty} \theta_i^t \frac{\psi_i(x)}{\rho(x)} \psi_i. \quad (24)$$

Now,

$$\begin{aligned} \|\Pi_{\text{span}\{\psi_0, \dots, \psi_d\}} (p_{x_1}^t - p_{x_2}^t)\|_{L^2_{1/\rho}}^2 &= \int_{\mathbb{X}} |\Pi_{\text{span}\{\psi_0, \dots, \psi_d\}} (p_{x_1}^t - p_{x_2}^t)(y)|^2 \frac{1}{\rho(y)} dy \\ &= \int_{\mathbb{X}} |\Pi_{\text{span}\{\psi_0, \dots, \psi_d\}} (p_{x_1}^t - p_{x_2}^t)(y)| \frac{|\Pi_{\text{span}\{\psi_0, \dots, \psi_d\}} (p_{x_1}^t - p_{x_2}^t)(y)|}{\rho(y)} dy. \end{aligned}$$

With (24), the second factor of the integrand can be estimated as follows:

$$\begin{aligned} \left| \frac{\Pi_{\text{span}\{\psi_0, \dots, \psi_d\}}(p_{x_1}^t - p_{x_2}^t)(y)}{\rho(y)} \right| &= \left| \sum_{i=0}^d \theta_i^t \left(\frac{\psi_i(x_1)}{\rho(x_1)} - \frac{\psi_i(x_2)}{\rho(x_2)} \right) \frac{\psi_i(y)}{\rho(y)} \right| \\ &\leq 2d \sup_{i=1, \dots, d} \|\psi_i / \rho\|_\infty^2. \end{aligned}$$

Thus, we finally get

$$\begin{aligned} \left\| \Pi_{\text{span}\{\psi_0, \dots, \psi_d\}}(p_{x_1}^t - p_{x_2}^t) \right\|_{L_{1/\rho}^2} &\leq \sqrt{2d} \sup_{i=0, \dots, d} \|\psi_i / \rho\|_\infty \int_{\mathbb{X}} \left| \Pi_{\text{span}\{\psi_0, \dots, \psi_d\}}(p_{x_1}^t - p_{x_2}^t)(y) \right| dy \\ &= \sqrt{2d} \sup_{i=0, \dots, d} \|\psi_i / \rho\|_\infty \left\| \Pi_{\text{span}\{\psi_0, \dots, \psi_d\}}(p_{x_1}^t - p_{x_2}^t) \right\|_{L^1} \\ &\leq \sqrt{2d} \sup_{i=0, \dots, d} \|\psi_i / \rho\|_\infty |\mathbb{X}| \left\| \Pi_{\text{span}\{\psi_0, \dots, \psi_d\}}(p_{x_1}^t - p_{x_2}^t) \right\|_{L^2}, \end{aligned}$$

where $\|f\|_{L^1} \leq |\mathbb{X}| \cdot \|f\|_{L^2}$ due to Hölder's inequality. \square